nature communications

Article

https://doi.org/10.1038/s41467-025-59897-7

Pressure tuning of competing interactions on a honeycomb lattice

Received: 19 March 2024

Accepted: 8 May 2025

Published online: 21 May 2025

Check for updates

Piyush Sakrikar[1,10], Bin Shen[2,10], Eduardo H. T. Poldi[3,4,10], Faranak Bahrami[1], Xiaodong Hu[1], Eric M. Kenney[1,5], Qiaochu Wang[6], Kyle W. Fruhling[1], Chennan Wang[7], Ritu Gupta[7], Rustem Khasanov[7], Hubertus Luetkens[7], Stuart A. Calder[8], Adam A. Aczel[8], Gilberto Fabbris[4], Russell J. Hemley[9], Kemp W. Plumb[6], Ying Ran[1], Philipp Gegenwart[2], Alexander A. Tsirlin[2], Daniel Haskel[4], Michael J. Graf[1] & Fazel Tafti[1]

Exchange interactions are mediated via orbital overlaps across chemical bonds. Thus, modifying the bond angles by physical pressure or strain can tune the relative strength of competing interactions. Here we present a remarkable case of such tuning between the Heisenberg (J) and Kitaev (K) exchange, which respectively establish magnetically ordered and spin liquid phases on a honeycomb lattice. We observe a rapid suppression of the Néel temperature (T_N) with pressure in $Ag_3LiRh_2O_6$, a spin-1/2 honeycomb lattice with both J and K couplings. Using a combined analysis of x-ray data and first-principles calculations, we find that pressure modifies the bond angles in a way that increases the $|K/J|$ ratio and thereby suppresses T_N. Consistent with this picture, we observe a spontaneous onset of muon spin relaxation (μSR) oscillations below T_N at low pressure, whereas in the high pressure phase, oscillations appear only when $T < T_N/2$. Unlike other candidate Kitaev materials, $Ag_3LiRh_2O_6$is tuned toward a quantum critical point by pressure while avoiding a structural dimerization in the relevant pressure range.

Materials with a honeycomb lattice and heavy elements can sustain anisotropic Kitaev interactions that favor a quantum spin liquid (QSL) ground state[1–3]. The same materials also host isotropic Heisenberg interactions that favor a long-range magnetic order (LRO)[4,5]. Theoretically, the QSL ground state could be established by tuning the competition between the Kitaev and Heisenberg interactions in favor of the former[6,7]. One approach to this problem would be to chemically design new materials with a large Kitaev to Heisenberg coupling ratio $|K/J|$. Unfortunately, this is proven to be an extremely challenging task[8–12]. An alternative approach would be to use external parameters such as magnetic field strength[13] or angle[14] to tune an existing material away from the Heisenberg limit and toward the Kitaev limit. In this work, we present a successful case of such tuning by applying hydrostatic pressure, instead of a magnetic field, on the honeycomb lattice of $Ag_3LiRh_2O_6$. Unlike all prior Kitaev materials, $Ag_3LiRh_2O_6$ avoids a structural dimerization at low pressures, providing a hitherto unavailable opportunity to investigate competing exchange interactions under pressure in a spin-1/2 honeycomb system.

$Ag_3LiRh_2O_6$ is synthesized from the parent compound Li_2RhO_3 by replacing the small interlayer Li atoms with large Ag atoms in a

[1]Department of Physics, Boston College, Chestnut Hill, MA 02467, USA. [2]Experimental Physics VI, Center for Electronic Correlations and Magnetism, University of Augsburg, 86159 Augsburg, Germany. [3]Departments of Physics, University of Illinois Chicago, Chicago, IL 60607, USA. [4]Advanced Photon Source, Argonne National Laboratory, Argonne, IL 60439, USA. [5]Muon Science Laboratory, Institute of Materials Structure Science, High Energy Accelerator Research Organization (KEK), Tsukuba, Ibaraki 305-0801, Japan. [6]Department of Physics, Brown University, Providence, RI 02912, USA. [7]PSI Center for Neutron and Muon Sciences CNM, 5232 Villigen PSI, Switzerland. [8]Neutron Scattering Division, Oak Ridge National Laboratory, Oak Ridge, TN 37831, USA. [9]Departments of Physics, Chemistry, and Earth and Environmental Sciences, University of Illinois Chicago, Chicago, IL 60607, USA. [10]These authors contributed equally: Piyush Sakrikar, Bin Shen, Eduardo H. T. Poldi. e-mail: fazel.tafti@bc.edu

topochemical exchange reaction (Fig. 1a)[15]. Changing the interlayer atoms induces a trigonal distortion in RhO_6 octahedra, which enhances the Ising-like anisotropy of the pseudospin-1/2 states[15]. As a result, a robust antiferromagnetic (AFM) order is established in $Ag_3LiRh_2O_6$ at T_N = 100 K, in stark contrast to the glassy transition at 6 K in Li_2RhO_3. The large T_N in $Ag_3LiRh_2O_6$ indicates a dominant Heisenberg interaction, i.e., a small $|K/J|$ ratio. We decided to study this material under pressure based on quantum chemistry calculations that predict the $|K/J|$ ratio could be increased by modifying the ∠Rh-O-Rh bond angles within the honeycomb layers (Fig. 1b)[16]. 4*d* transition metal systems such as Li_2RhO_3 and $Ag_3LiRh_2O_6$ are particularly sensitive to changes of bond angles, since they have comparable spin–orbit coupling and crystal field energy scales[17].

Our multiprobe investigations reveal three pieces of evidence for a shift in the balance between the Heisenberg and Kitaev interactions with increasing pressure in $Ag_3LiRh_2O_6$. (i) Magnetization measurements show a rapid suppression of T_N under pressure up to 3 GPa, beyond which, the AFM order disappears. (ii) X-ray diffraction (XRD) confirms the absence of structural transitions up to 5 GPa, beyond which, the honeycomb lattice undergoes a dimerization transition. (iii) μSR experiments reveal a long-range order below T_N at low pressures but a short-range order at high pressures, which becomes long-range only when $T < T_N/2$. Thus, the μSR data indicate an extended temperature regime of fluctuating short-range magnetism. Details of the magnetization, XRD, and μSR data are presented below.

Magnetization

We started the high-pressure investigations of $Ag_3LiRh_2O_6$ by measuring the DC magnetic susceptibility of a polycrystalline sample inside a ceramic anvil pressure cell. To reach the maximum pressure of about 5.5 GPa, we used a pair of anvils with small culets in runs 1, 2 and 3 (Methods). To obtain higher quality data for the Curie–Weiss (CW) analysis, we used another pair of anvils with larger culets which limited the pressure to 2 GPa in run 4.

The first observation in Fig. 1c is a rapid suppression of T_N with pressure at a rate of −20 K/GPa up to about 3 GPa. At each pressure, T_N was obtained from the peak in the $\chi(T)$ curve as seen in Fig. 1d for run 4. The high quality of these data enabled us to perform Curie–Weiss (CW) fits to extract the CW temperature (Θ_{CW}) and effective magnetic moment (μ_{eff}). Plotting T_N, Θ_{CW}, and μ_{eff} as a function of pressure in Fig. 1e reveals a parallel suppression of T_N and Θ_{CW} with pressure, while μ_{eff} remains nearly unchanged. Since Θ_{CW} is proportional to the Heisenberg coupling J, the parallel suppression of Θ_{CW} and T_N indicates a weakening of the average J under pressure. The value of $\mu_{eff} \approx 1.9\ \mu_B$, which is unaffected by pressures, is close to the expected moment for a pseudospin-1/2 state. In the supplementary information, we also provide DFT results that confirm the robustness of the pseudospin-1/2 state up to 5 GPa. These observations suggest that while the pseudospin-1/2 state in $Ag_3LiRh_2O_6$ remains unchanged under pressure, the Heisenberg interactions weaken with increasing pressure, resulting in a rapid suppression of T_N.

Switching to anvils with smaller culet sizes, we extended measurements of $\chi(T)$ to higher pressures in runs 1, 2, and 3 (Fig. 1f and the supplementary Fig. S1). The $\chi(T)$ curves qualitatively changed at $P > 3$ GPa, where the AFM peak became smaller in magnitude and nearly disappeared at $P > 4$ GPa (Fig. 1f). The disappearance of the AFM peak at high pressures suggests that the Kitaev coupling K is suppressed at a slower rate than Heisenberg coupling J, hence the ratio $|K/J|$ is enhanced with increasing pressure.

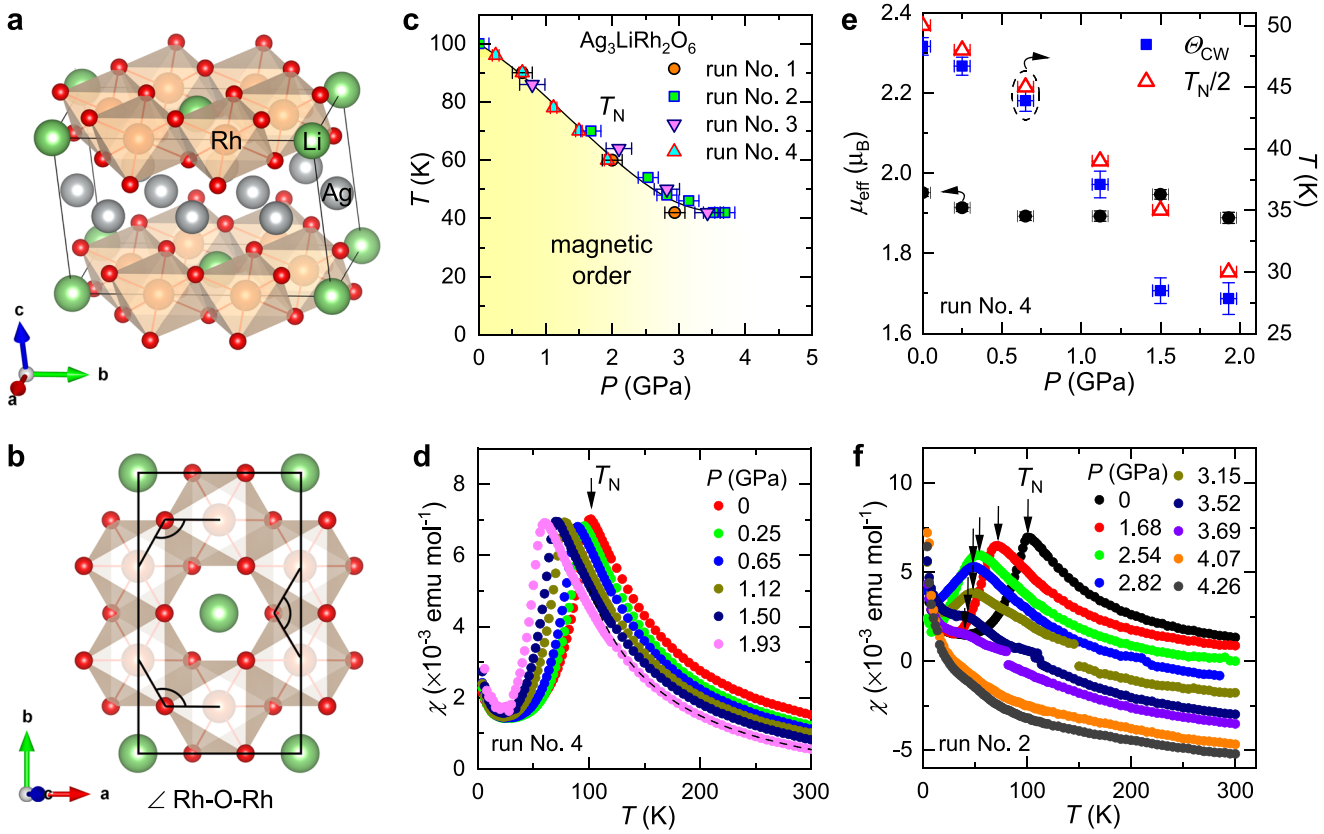

Fig. 1 | Magnetization data. a Unit cell of $Ag_3LiRh_2O_6$ in the monoclinic space group *C*2/*m* with Ag atoms between the [$LiRh_2O_6$] honeycomb layers. **b** ∠Rh-O-Rh bond angles within a honeycomb layer. **c** Suppression of T_N with increasing pressure. **d** T_N is identified by the peak in $\chi(T)$ at different pressures. **e** Both T_N and Θ_{CW} decrease in parallel with pressure while μ_{eff} remains nearly unchanged. All data in this panel are from run No. 4. **f** The peak in susceptibility data (T_N) disappears at $P > 4$ GPa.

https://doi.org/10.1038/s41467-025-59897-7

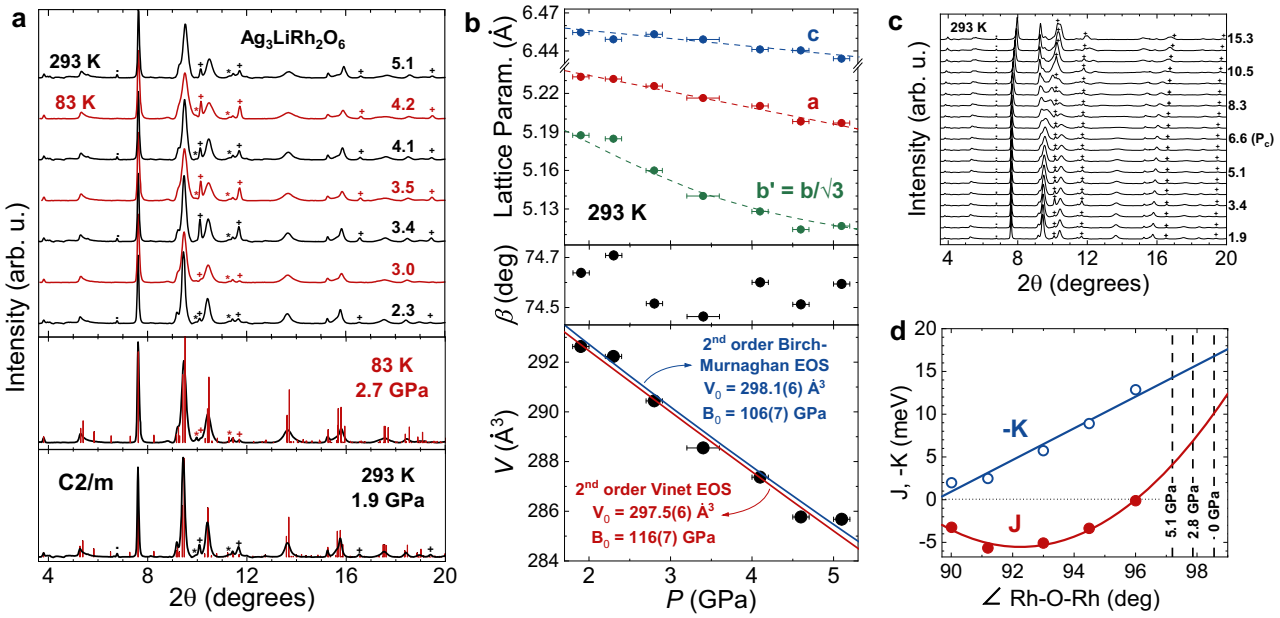

Fig. 2 | X-ray diffraction. a Pressure-dependent diffraction patterns at 293 K (black) and 83 K (red). The *, +, and . symbols indicate, respectively, the Re peaks (gasket), Au peaks (manometer), and boron carbide seat. Red vertical bars in the bottom panel indicate calculated Bragg peak intensities at 1.9 GPa (293 K) and 2.7 GPa (83 K). **b** Monoclinic unit cell parameters, angle β, and volume plotted as a function of pressure. The *P-V* data are fitted (solid lines) using both second-order Vinet and second-order Birch–Murnaghan equations of state, rendering comparable values for the bulk modulus (B_0) and ambient pressure volume (V_0). **c** The bifurcation of the 9.5° Bragg peak at P_c = 6.6 GPa indicates a dimerization transition (see also Fig. S2). **d** The linear and quadratic dependence of *K* and *J* on ∠Rh-O-Rh are reproduced from ref. 16. Dashed lines indicate the average bond angle at different pressures.

X-ray diffraction

We performed XRD measurements under pressure with two goals in mind. First, to confirm that the suppression of the AFM order was not due to a structural transition, and second, to correlate the T_N suppression with a change of ∠Rh-O-Rh bond angle.

Our search for a pressure-induced structural transition was motivated by previous studies on the hyper-honeycomb system β-Li_2IrO_3, which similar to $Ag_3LiRh_2O_6$, has a high T_N of 38 K at ambient pressure and loses its AFM order under pressure[18–21]. However, unlike in $Ag_3LiRh_2O_6$, T_N remains nearly independent of pressure in β-Li_2IrO_3 until the AFM order disappears abruptly at P_c = 1.4 GPa[20,21]. The sudden loss of the AFM order in β-Li_2IrO_3 is unrelated to competing interactions. Instead, it originates form the loss of local moments due to the formation of Ir_2 dimers under pressure[19–21]. Measurements of x-ray magnetic circular dichroism (XMCD)[19] revealed a quenching of both spin and orbital moments due to this dimerization at P_c = 1.4 GPa. Thus, we performed high-pressure x-ray diffraction on $Ag_3LiRh_2O_6$ to distinguish between two mechanisms for the loss of AFM order: (i) structural dimerization, and (ii) competing interactions.

The XRD patterns in Fig. 2a show that the monoclinic *C*2/*m* structure is preserved in $Ag_3LiRh_2O_6$ from 0 to 5 GPa at both 293 and 85 K. The Bragg peaks are slightly broadened with increasing pressure due to the loss of hydrostatic conditions. However, the amount of stacking faults is not changed considerably as evidenced by a nearly unchanged Warren line shape[22] between 5 and 6 degrees (see the supplementary Fig. S3). In similar compounds such as Li_2RhO_3 and Cu_2IrO_3, the stacking faults are in fact reduced under pressure[23,24]. Thus, increasing stacking faults is not responsible for the T_N suppression in $Ag_3LiRh_2O_6$.

Using Le Bail fits to these data, we trace the evolution of the unit cell parameters with pressure in Fig. 2b. All lattice parameters are smoothly decreasing with increasing pressure, and the monoclinic angle β fluctuates around 74.6(1) degrees. The absence of a structural transition up to 5 GPa in Figs. 2a, b rules out the dimerization of Rh_2 units as the mechanism of T_N suppression. This is consistent with the pressure independent μ_{eff} in Fig. 1e, since the formation of Rh_2 dimers would have quenched the local moments.

Figure 2c shows that a structural transition finally occurs at P_c = 6.6(5) GPa, well above the pressure range of T_N suppression in Fig. 1c. The structural transition is signaled by a bifurcation of the Bragg peak at 9.5° in Fig. 2c (see also supplementary Fig. S2). A similar dimerization transition has been reported in Li_2RhO_3 at nearly the same critical pressure[23].

The known presence of stacking faults in $Ag_3LiRh_2O_6$[15] and the limited angular range of the high-pressure XRD data made Rietveld refinements of atomic positions challenging. Instead, we used the lattice parameters from XRD as input to a density functional theory (DFT) code and found the atomic positions that minimized the free energy (supplementary information). Using the atomic coordinates from DFT, we evaluated the ∠Rh-O-Rh bond angles at high pressures. The three dashed lines in Fig. 2d indicate the average values of ∠Rh-O-Rh at different pressures, overlaid on a plot of *J* and *K* couplings versus ∠Rh-O-Rh according to quantum chemistry calculations in Li_2RhO_3[16]. The key observation is that $|K/J|$ ratio increases rapidly with increasing pressure as the bond angles approach the critical value of 96° where $J \to 0$. Note that *J* changes quadratically with bond angle while $|K|$ changes linearly. This leads to the rapid increase of $|K/J|$ from 1.6 to 2.6 and 3.6 as the pressure increases from 0 to 2.8 and 5.1 GPa, respectively. Such enhancement of the $|K/J|$ ratio in the absence of a structural transition before 5.5 GPa suggests that competing interactions are responsible for the T_N suppression and disappearance of the AFM peak in Fig. 1.

We used the calculated *J* and *K* curves for Li_2RhO_3 in Fig. 2d, because such calculations do not exist for $Ag_3LiRh_2O_6$ at present. However, the 2D layers of $Ag_3LiRh_2O_6$ are similar to Li_2RhO_3, justifying our approach. Future material-specific calculations will be necessary for a quantitative analysis. Nevertheless, the analysis in Fig. 2d demonstrates how competing Kitaev and Heisenberg interactions could lead to the suppression of the AFM order.

https://doi.org/10.1038/s41467-025-59897-7

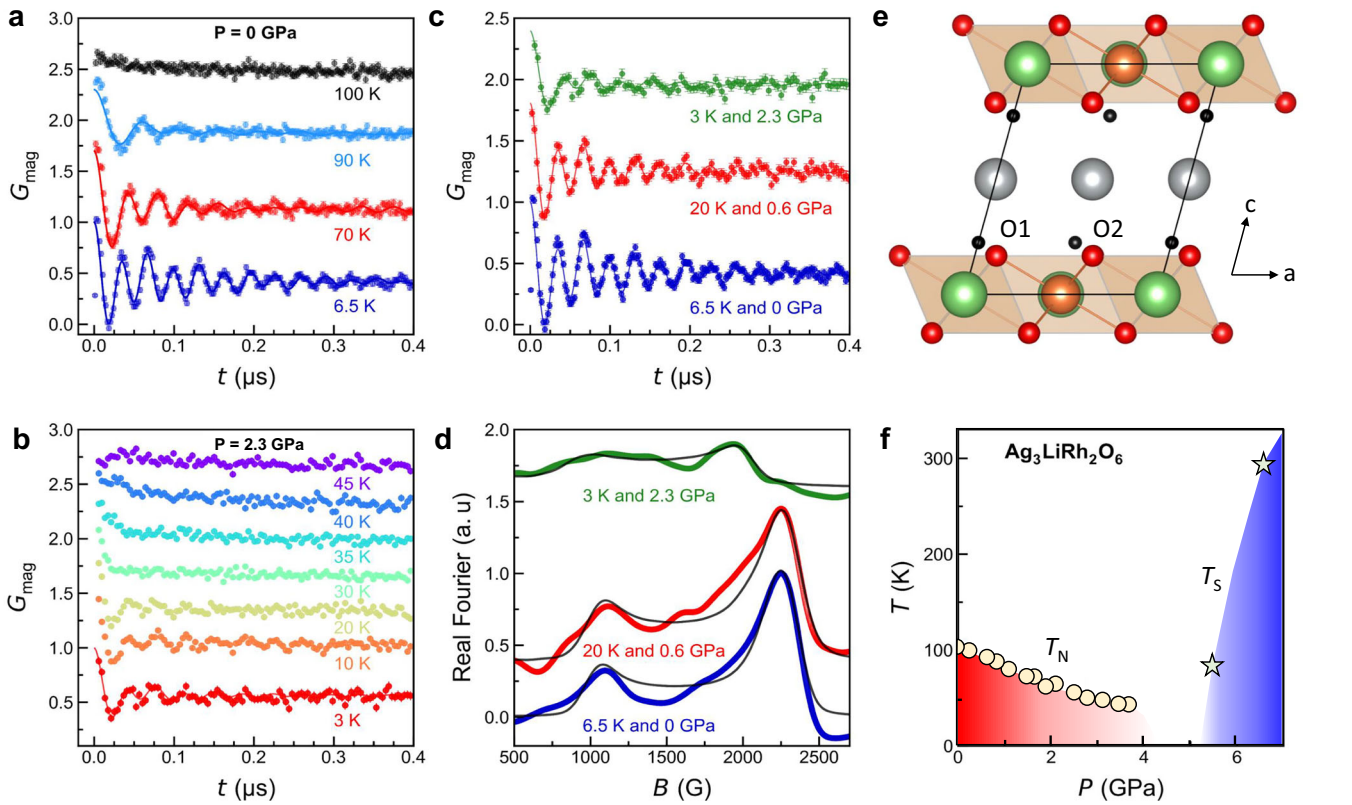

Fig. 3 | μSR data. a Muon polarization at a low pressure showing oscillations immediately below T_N. **b** At high pressure, oscillations do not appear until $T_N/2$. **c** Comparing the low-T polarization curves at low-pressure (0 and 0.6 GPa) and high-pressure (2.3 GPa). **d** Comparing the Fourier transforms of polarization curves. **e** Visualizing the muon stopping sites (black circles near each oxygen site) in the lattice structure. **f** Phase diagram of the magnetic (T_N) and structural (T_S) transitions shown by circles and stars, respectively. The red and blue shades correspond to the disappearance of the magnetic order and the appearance of the structural dimerization.

Muon spin relaxation

In μSR, positively charged spin-polarized muons are implanted in a sample to probe the local magnetic field at some preferred crystallographic stopping site(s). The average time evolution of the muon polarization $G(t)$ is monitored by detection of positrons which are preferentially emitted along the muon polarization direction upon its decay (lifetime τ = 2.2 μs). Long-range magnetic order is signaled by the onset of oscillations in $G(t)$ in zero magnetic field, and decay of $G(t)$ (depolarization) can be caused by either magnetic disorder or dynamical fluctuations. The polarization curves in Fig. 3 are labeled $G_{mag}(t)$ to indicate the removal of background signal from the pressure cell[25] and a small non-magnetic signal from silver inclusions in the sample from the total polarization signal $G(t)$. Details of background subtraction are given in the supplementary information (Fig. S4).

Before presenting any quantitative analysis, we reveal a qualitative difference between $G_{mag}(t)$ curves obtained at low-pressure (P < 2 GPa) and high-pressure (P > 2 GPa) in Figs. 3a, b. Whereas the oscillations appear immediately below T_N = 95 K at P = 0 (Fig. 3a), they do not appear until the temperature is decreased to half the T_N = 43 K at P = 2.3 GPa (Fig. 3b). The observation of spontaneous oscillations below T_N at low pressures (Fig. 3a) indicates the onset of long-range ordering. This is a typical behavior in a sample without magnetic disorder. The surprising result is that at high pressures (Fig. 3b), oscillations associated with a long-range order do not appear until temperatures below 20 K, which is half the T_N = 42 K at 2.3 GPa (Fig. 1c). In the intermediate range $\frac{T_N}{2} < T < T_N$, oscillations are replaced with a fast depolarization, suggesting short-range magnetic ordering. A similar behavior has been reported at ambient pressure in Li_2RhO_3 and α-Li_2IrO_3, which are proximate Kitaev spin liquid materials[16,26,27]. Thus, pressure tunes the long-range AFM order in $Ag_3LiRh_2O_6$ toward the short-range order observed in its parent compound Li_2RhO_3.

In addition to the qualitative differences between low-pressure and high-pressure polarization curves at $\frac{T_N}{2} < T < T_N$, we also find quantitative differences at $T \ll T_N$. Figures 3c, d show $G_{mag}(t)$ spectra and their Fourier transforms at ambient pressure, 0.6 GPa, and 2.3 GPa for $T \leq 10$ K. We fit the magnetic polarization curves to the following expression

$$\begin{aligned} G_{mag}(t) = f_{osc}\Big[& f_1 J_0(\gamma_\mu \Delta B_1 t)\cos(\gamma_\mu B_{1,avg} t)\exp(-\Lambda_1 t) \\ & + f_2 J_0(\gamma_\mu \Delta B_2 t)\cos(\gamma_\mu B_{2,avg} t)\exp(-\Lambda_2 t)\Big] \\ & + (1 - f_{osc})\exp(-\lambda_L t) \end{aligned} \quad (1)$$

which consists of two oscillatory terms, indicating two inequivalent muon stopping sites. The two stopping sites were calculated by minimizing electrostatic potential near each crystallographically distinct oxygen site (O_1 and O_2) in the unit cell (Fig. 3e). Each term in Eq. (1) has a fractional contribution (f_1 and f_2) to the total oscillatory component f_{osc} constrained by $f_1 + f_2 = 1$; f_{osc} was found to be 0.59(1) at low temperature and ambient pressure and fixed at that value in all subsequent fits. f_1 and f_2 were 0.6 and 0.4, respectively, at low temperatures. The two oscillatory terms are known as the Overhauser approximation[28] for incommensurate magnetic ordering (consistent with neutron scattering data in the SI) with a field distribution experienced by the muon which is symmetric about some non-zero average field in the range $B_{i,min} \leq B_i \leq B_{i,max}$, with

$$B_{i,avg} = \frac{B_{i,max} + B_{i,min}}{2}, \quad \Delta B_i = \frac{B_{i,max} - B_{i,min}}{2} \quad (2)$$

Table 1 | Fit parameters from Eq. (1) at ambient, low, and high pressures for $T \ll T_N$

Pressure	0 GPa	0.6 GPa	2.3 GPa
T_N (K)	95.3 (2)	95.4 (8)	42.7 (2)
$B_{1,\,min}$ (G)	1010 (14)	1023 (22)	14 (3)
$B_{1,\,max}$ (G)	2134 (14)	2155 (22)	2010 (3)
$B_{2,\,min}$ (G)	2193 (14)	2203 (13)	832 (56)
$B_{2,\,max}$ (G)	2335 (4)	2335 (13)	1922 (56)
Λ_1 (μs^{-1})	2.6 (4)	4 (1)	0.2 (1)
Λ_2 (μs^{-1})	2.2 (2)	4.4 (8)	7 (3)
f_{osc}	0.58 (1)	0.55 (3)	0.48 (3)

Although the AFM transition appears sharper in the magnetization data, we use μSR fits (Figs. S4b, S5b) to report T_N values in this Table, so that all parameters are extracted from the same measurement. A graphical summary of the pressure dependence of local fields is presented in Fig. S6.

and J_0 being the zeroth-order Bessel function of the first kind. Each term in Eq. (1) is damped at a respective rate Λ_i. A long-time exponential decay with the rate λ_L constitutes the remaining fraction of the $Ag_3LiRh_2O_6$ response from the muons that experience a local field parallel to the initial muon spin orientation (on average 1/3 of the muons in an isotropic polycrystalline sample). For ease of fitting, we only used a single λ_L for both muon stopping sites. The fit parameters at low- and high-pressure regimes are listed in Table 1. We note that f_{osc} is somewhat less than 0.67 expected for an isotropic polycrystalline sample, suggesting a small degree of preferred orientation in the pressed polycrystalline pellet. Also, beamline optimization between measurements at different pressures could lead to slightly lower f_{osc} at 2.3 GPa. Such optimizations are necessary as the sample volume and its precise location in the cryostat change between different pressure runs.

While T_N is substantially reduced by the application of 2.3 GPa, consistent with the magnetization data, we find small changes in the local field parameters $B_{1,\,max}$ and $B_{2,\,max}$. Such modest changes of the upper limits on the local field (less than 20%) could be accounted for by small changes of lattice parameters with pressure (Fig. 2b), which change the local field experienced by muons at the stopping sites (Fig. 3e). The small change of local fields in μSR is consistent with the nearly unchanged magnetic moment under pressure in the Curie–Weiss analysis (Fig. 1e). These observations show the presence of robust local moments despite weakening of the magnetic order at high pressures, consistent with increasing $|K/J|$ ratio.

Discussion

In previous studies,[13,14] magnetic field has been used to melt the long-range order into a fluctuating regime in honeycomb lattices such as α-$RuCl_3$. Instead of changing the strength of J or K couplings, the magnetic field enters the Hamiltonian as an external parameter (Zeeman term)[29,30]. In contrast, pressure tunes the relative strength of competing interactions directly, by changing orbital overlaps. Despite theoretical proposals about using pressure as a powerful tuning parameter in Kitaev systems[31,32], an experimental verification has not been possible until now, because a small pressure is enough to induce a dimerization transition in both 4d systems (Ru_2 dimerization at 0.2 GPa in α-$RuCl_3$ and at 0.5 GPa in $Ag_3LiRu_2O_6$)[33–36] and 5d systems (Ir_2 dimerization at 1.4 GPa in β-Li_2IrO_3)[19]. Remarkably, such a structural transition does not appear in $Ag_3LiRh_2O_6$ until 5 GPa, leaving a gap between the AFM (red) and dimerized (blue) phases in the phase diagram of Fig. 3f.

This work introduces $Ag_3LiRh_2O_6$ as a unique Kitaev material that avoids structural dimerization under pressure while the magnetic correlations change from long-range to short-range. It opens the possibility of tuning Kitaev and Heisenberg interactions as demonstrated in Fig. 2d. Such a possibility was not offered by other Kitaev materials so far, as they all dimerized at low pressures. Moving forward, it will be helpful to get spectroscopic information from inelastic x-ray scattering and Raman scattering about the pressure-induced quantum critical regime near 4 GPa, and to search for evidence of quantum critical behavior by measuring temperature dependence of specific heat or NMR at low temperatures ($T < 2$ K) near 4 GPa. Material specific calculations will be necessary to carefully investigate the tuning of Kitaev, Heisenberg, and off-diagonal exchange (Γ) interactions under pressure. The combination of such experimental and theoretical studies could reveal the nature of the low-lying excitations in the gap between the red and blue regimes in Fig. 3f.

Methods

Material synthesis

Polycrystalline samples of $Ag_3LiRh_2O_6$ were synthesized using a topochemical cation-exchange reaction from the parent compound Li_2RhO_3 following a previous publication[15]. The structural and compositional quality of all samples were characterized at ambient conditions with powder X-ray diffraction and energy dispersive X-ray spectroscopy. The only impurity found was about 5% silver inclusions.

Magnetization measurements

Magnetization of the powder sample was measured in a Quantum Design MPMS3 using a composite ceramic anvil cell[37] with Daphne oil 7373 as the pressure-transmitting medium. Pressure was determined from the superconducting transition of a lead manometer. To achieve the maximum pressure of about 5.5 GPa, a pair of anvils with small culet sizes (1 mm) were used in runs 1, 2, and 3. A small sample chamber with both diameter and thickness of 0.5 mm was drilled into the Be-Cu gasket. To obtain data with higher quality for the CW fits, another pair of anvils with larger culets (1.8 mm) were used in run 4. This time, the maximum pressure was about 2 GPa due to the larger sample chamber with both diameter and thickness of 0.9 mm. In each run, the magnetization of the empty cell was measured first as the background and subtracted from the total signal. The small jumps near zero magnetization in Fig. 1f and Fig. S1a, b are due to this subtraction.

Muon spin relaxation (μSR)

The μSR experiments were performed at the Paul Scherrer Institute using the General Purpose Surface-Muon (GPS) and General Purpose Decay-Channel (GPD) spectrometers on the "πM3" and "μE1" beamlines, respectively. Measurements on a pressed disk (12-mm diameter, 1-mm thickness) were made on GPS at ambient pressure using a gas flow cryostat between 110 and 6.5 K. Measurements in GPD at pressures of 0.57 and 2.29 GPa (as determined by an indium manometer) were made in a He-flow cryostat using a piston-cylinder pressure cell[25] with Daphne oil 7373 as the pressure-transmitting medium. Data were analyzed using the MUSRFIT program[38].

X-ray diffraction

X-ray diffraction (XRD) data were collected at the High Pressure Collaborative Access Team (HPCAT) beamline 16-BM-D of the Advanced Photon Source using diamond anvil cells (DAC) with a combination of full and partially perforated anvils to reduce x-ray attenuation. Anvil culet diameter was 300 μm. Rhenium gaskets were pre-indented to a thickness of 50 μm, and a 180-μm-diameter sample chamber was laser drilled at the center of the indentation. Fine powder (5 μm) of $Ag_3LiRh_2O_6$, together with ruby and gold manometers, were loaded into the sample chamber filled with Ne pressure medium. The entire sample chamber was rastered over the 25 × 25 μm^2 area of the 30 keV X-ray beam to improve powder averaging on the CCD detector. Measurements were carried out at both ambient and low temperature (83 K). 2D XRD images were integrated over 2π using Dioptas

software[39] and the integrated diffractograms were Le Bail fitted using Jana2020[40]. Pressure-dependent lattice parameters were extracted and second-order Vinet and Birch–Murnagham equations of state were both fitted using EoSFit[41].

DFT calculations

Structural optimization and electronic structure calculations at high pressures were performed using the QUANTUM ESPRESSO and Wannier90 codes[42–44] with the experimental crystallographic information as the input. To evaluate the wavefunctions in the supplementary information (Table S1), we first used Quantum ESPRESSO and Wannier90 codes to compute the electronic structure using experimental lattice parameters from our XRD measurements under pressure. Then, a tight-binding model was constructed for an individual RhO_6 cluster, defined by real-space hopping parameters extracted from DFT. The orbital information were calculated from a Hartree–Fock mean-field model.

Neutron diffraction

Neutron powder diffraction (NPD) was performed on 2 g of polycrystalline $Ag_3LiRh_2O_6$ using the HB-2A powder diffractometer and the HB-1A[45] triple-axis spectrometer (VERITAS) at the high flux isotope reactor (HFIR) at Oak Ridge National Laboratory (ORNL). On HB-2A, the sample was loaded into a 5-mm diameter Al can to give an overall neutron transmission of 77.67%. We used collimations of open-21′-12′ with a wavelength of 2.41 Å. On HB-1A, the sample was loaded into an annular can with a 1-mm annulus and resulting neutron transmission of 90.38%. We used collimations of 40′-40′-40′-80′ with a fixed incident energy of 14.5 meV. FULLPROF[46] was used for Rietveld refinements of crystal structures and computing predicted magnetic diffraction patterns to compare with experimental data.

Data availability

All data in this work are published online and available in the ref. 47.

References

1. Jackeli, G. & Khaliullin, G. Mott insulators in the strong spin-orbit coupling limit: from Heisenberg to a quantum compass and Kitaev models. *Phys. Rev. Lett.* **102**, 017205 (2009).
2. Chaloupka, J., Jackeli, G. & Khaliullin, G. Kitaev-Heisenberg model on a honeycomb lattice: possible exotic phases in iridium oxides A_2IrO_3. *Phys. Rev. Lett.* **105**, 027204 (2010).
3. Takagi, H., Takayama, T., Jackeli, G., Khaliullin, G. & Nagler, S. E. Concept and realization of Kitaev quantum spin liquids. *Nat. Rev. Phys.* **1**, 264–280 (2019).
4. Singh, Y. et al. Relevance of the Heisenberg-Kitaev model for the honeycomb lattice iridates A_2IrO_3. *Phys. Rev. Lett.* **108**, 127203 (2012).
5. Chaloupka, J., Jackeli, G. & Khaliullin, G. Zigzag magnetic order in the iridium oxide Na_2IrO_3. *Phys. Rev. Lett.* **110**, 097204 (2013).
6. Rau, J. G., Lee, E. K.-H. & Kee, H.-Y. Generic spin model for the honeycomb iridates beyond the Kitaev limit. *Phys. Rev. Lett.* **112**, 077204 (2014).
7. Kimchi, I. & Vishwanath, A. Kitaev-Heisenberg models for iridates on the triangular, hyperkagome, kagome, fcc, and pyrochlore lattices. *Phys. Rev. B* **89**, 014414 (2014).
8. Winter, S. M., Li, Y., Jeschke, H. O. & Valentì, R. Challenges in design of Kitaev materials: magnetic interactions from competing energy scales. *Phys. Rev. B* **93**, 214431 (2016).
9. Winter, S. M. et al. Models and materials for generalized Kitaev magnetism. *J. Phys. Condens. Matter* **29**, 493002 (2017).
10. Bahrami, F. et al. Effect of structural disorder on the Kitaev magnet $Ag_3LiIr_2O_6$. *Phys. Rev. B* **103**, 094427 (2021).
11. Kenney, E. M. et al. Coexistence of static and dynamic magnetism in the Kitaev spin liquid material Cu_2IrO_3. *Phys. Rev. B* **100**, 094418 (2019).
12. Kitagawa, K. et al. A spin-orbital-entangled quantum liquid on a honeycomb lattice. *Nature* **554**, 341–345 (2018).
13. Banerjee, A. et al. Excitations in the field-induced quantum spin liquid state of α-$RuCl_3$. *npj Quantum Mater.* **3**, 1–7 (2018).
14. Tanaka, O. et al. Thermodynamic evidence for a field-angle-dependent Majorana gap in a Kitaev spin liquid. *Nat. Phys.* **18**, 429–435 (2022).
15. Bahrami, F. et al. First demonstration of tuning between the Kitaev and Ising limits in a honeycomb lattice. *Sci. Adv.* **8**, eabl5671 (2022).
16. Katukuri, V. M. et al. Strong magnetic frustration and anti-site disorder causing spin-glass behavior in honeycomb Li_2RhO_3. *Sci. Rep.* **5**, 14718 (2015).
17. Katukuri, V. M. et al. Electronic structure of low-dimensional $4d^5$ oxides: interplay of ligand distortions, overall lattice anisotropy, and spin-orbit interactions. *Inorg. Chem.* **53**, 4833–4839 (2014).
18. Takayama, T. et al. Hyperhoneycomb iridate β-Li_2IrO_3 as a platform for Kitaev magnetism. *Phys. Rev. Lett.* **114**, 077202 (2015).
19. Veiga, L. S. I. et al. Pressure tuning of bond-directional exchange interactions and magnetic frustration in the hyperhoneycomb iridate β-Li_2IrO_3. *Phys. Rev. B* **96**, 140402 (2017).
20. Majumder, M. et al. Breakdown of magnetic order in the pressurized Kitaev iridate β-Li_2IrO_3. *Phys. Rev. Lett.* **120**, 237202 (2018).
21. Shen, B. et al. Interplay of magnetism and dimerization in the pressurized Kitaev material *beta*-Li_2IrO_3. *Phys. Rev. B* **104**, 134426 (2021).
22. Abramchuk, M. et al. Crystal chemistry and phonon heat capacity in quaternary honeycomb delafossites: $Cu[Li_{1/3}Sn_{2/3}]O_2$ and $Cu[Na_{1/3}Sn_{2/3}]O_2$. *Inorg. Chem.* **57**, 12709–12717 (2018).
23. Hermann, V. et al. Pressure-induced formation of rhodium zigzag chains in the honeycomb rhodate Li_2RhO_3. *Phys. Rev. B* **100**, 064105 (2019).
24. Fabbris, G. et al. Complex pressure-temperature structural phase diagram of the honeycomb iridate Cu_2IrO_3. *Phys. Rev. B* **104**, 014102 (2021).
25. Khasanov, R. Perspective on muon-spin rotation/relaxation under hydrostatic pressure. *J. Appl. Phys.* **132**, 190903 (2022).
26. Khuntia, P. et al. Local magnetism and spin dynamics of the frustrated honeycomb rhodate Li_2RhO_3. *Phys. Rev. B* **96**, 094432 (2017).
27. Choi, S. et al. Spin dynamics and field-induced magnetic phase transition in the honeycomb Kitaev magnet α-Li_2IrO_3. *Phys. Rev. B* **99**, 054426 (2019).
28. Amato, A. et al. Understanding the μSR spectra of MnSi without magnetic polarons. *Phys. Rev. B* **89**, 184425 (2014).
29. Zhang, S.-S., Halász, G. B. & Batista, C. D. Theory of the Kitaev model in a [111] magnetic field. *Nat. Commun.* **13**, 399 (2022).
30. Cônsoli, P. M., Janssen, L., Vojta, M. & Andrade, E. C. Heisenberg-Kitaev model in a magnetic field: 1/*S* expansion. *Phys. Rev. B* **102**, 155134 (2020).
31. Yadav, R., Rachel, S., Hozoi, L., van den Brink, J. & Jackeli, G. Strain- and pressure-tuned magnetic interactions in honeycomb Kitaev materials. *Phys. Rev. B* **98**, 121107 (2018).
32. Bhattacharyya, P. et al. Maximized K/J ratio and cubiclike jeff = 1/2 moments in a noncubic environment in RuCl3 under pressure. *Phys. Rev. B* **108,** L161107 (2023).
33. Bastien, G. et al. Pressure-induced dimerization and valence bond crystal formation in the Kitaev-Heisenberg magnet α-$RuCl_3$. *Phys. Rev. B* **97**, 241108 (2018).
34. Stahl, Q. et al. Pressure-tuning of $RuCl_3$ towards the ideal Kitaev-limit. *Nat. Commun.* **15**, 8142 (2024).
35. Wang, Z. et al. Pressure-induced melting of magnetic order and emergence of a new quantum state in α-$RuCl_3$. *Phys. Rev. B* **97**, 245149 (2018).
36. Takayama, T. et al. Competing spin-orbital singlet states in the $4d^4$ honeycomb ruthenate $Ag_3LiRu_2O_6$. *Phys. Rev. Res.* **4**, 043079 (2022).
37. Tateiwa, N., Haga, Y., Fisk, Z. & Ōnuki, Y. Miniature ceramic-anvil high-pressure cell for magnetic measurements in a commercial

superconducting quantum interference device magnetometer. *Rev. Sci. Instrum.* **82**, 053906 (2011).
38. Suter, A. & Wojek, B. M. Musrfit: a free platform-independent framework for μSR data analysis. *Phys. Procedia* **30**, 69–73 (2012).
39. Prescher, C. & Prakapenka, V. B. DIOPTAS: a program for reduction of two-dimensional X-ray diffraction data and data exploration. *High. Press. Res.* **35**, 223–230 (2015).
40. Petr^íček, V., Palatinus, L., Plášil, J. & Dušek, M. Jana2020 - a new version of the crystallographic computing system Jana. Z. f.ür. *Kristallogr. Crystal. Mater.* **238**, 271–282 (2023).
41. Gonzalez-Platas, J., Alvaro, M., Nestola, F. & Angel, R. EosFit7-GUI: a new graphical user interface for equation of state calculations, analyses and teaching. *J. Appl. Crystallogr.* **49**, 1377–1382 (2016).
42. Giannozzi, P. et al. Quantum espresso: a modular and open-source software project for quantum simulations of materials. *J. Phys. Condens. matter* **21**, 395502 (2009).
43. Giannozzi, P. et al. Advanced capabilities for materials modelling with quantum espresso. *J. Phys. Condens. Matter* **29**, 465901 (2017).
44. Pizzi, G. et al. Wannier90 as a community code: new features and applications. *J. Phys. Condens. Matter* **32**, 165902 (2020).
45. Aczel, A. A. et al. Revisiting the Kitaev material candidacy of Ir^{4+} double perovskite iridates. *Phys. Rev. B* **99**, 134417 (2019).
46. Rodríguez-Carvajal, J. Recent advances in magnetic structure determination by neutron powder diffraction. *Phys. B Condens. Matter* **192**, 55–69 (1993).
47. Sakrikar, P. et al. Pressure tuning of competing interactions on a honeycomb lattice. *The Mater Data Facility*, https://doi.org/10.18126/4gwk-2m53 (2025).

Acknowledgements

The authors thank L. Hozoi for fruitful discussions. The work at Boston College was funded by the US Department of Energy, Office of Basic Energy Sciences, Division of Physical Behavior of Materials under award number DE-SC0023124. The work in Augsburg was funded by the Deutsche Forschungsgemeinschaft (DFG, German Research Foundation)—TRR 360-492547816. Bin Shen acknowledges the financial support of the Alexander von Humboldt Foundation. K.W.P. and Q.W. were supported by the US Department of Energy, Office of Basic Energy Sciences, under Grant No. DE-SC0021223. This work is based in part on experiments performed at the Swiss Muon Source SμS, Paul Scherrer Institute, Villigen, Switzerland. Neutron scattering experiments were carried out at the High Flux Isotope Reactor and Spallation Neutron Source, a DOE Office of Science User Facility operated by the Oak Ridge National Laboratory. Y.R. and X.H. acknowledge support from the National Science Foundation under Grant No. DMR-1712128. E.P. and R.J.H. acknowledge support from DOE-SC (DE-SC0020340), DOE-NNSA (DE-NA0003975), and NSF (DMR-2118020 and DMR-2119308). Operations of HPCAT (Sector 16, APS, ANL) are supported by DOE-NNSA's Office of Experimental Sciences. Work at the Advanced Photon Source was supported by the US Department of Energy Office of Science, Office of Basic Energy Sciences, under Award No. DE-AC02-06CH11357.

Author contributions

P.S., C.W., E.M.K., R.G., R.K., H.L., and M.J.G. performed μSR experiments. B.S., K.W.F., P.G., and A.A.T. performed magnetization measurements. E.D.T.P., G.F., R.J.H., and D.H. performed x-ray diffraction. Q.W., S.A.C., A.A.A., and K.W.P. performed neutron diffraction. F.B. synthesized the material. X.H. and Y.R. performed theoretical calculations. F.T. conceptualized and coordinated the project. All authors participated in the writing process.

Competing interests

The authors declare no competing interests.

Ethics

Contributions from all authors, including local scientists at the national and international labs, are properly acknowledged in this work.

Additional information

Supplementary information The online version contains supplementary material available at https://doi.org/10.1038/s41467-025-59897-7.

Correspondence and requests for materials should be addressed to Fazel Tafti.

Peer review information *Nature Communications* thanks the anonymous, reviewers for their contribution to the peer review of this work. A peer review file is available.